

High Dynamic Range Power Consumption Measurement in Microcontroller Based Applications

Attilio Di Nisio, *Member, IEEE*, Tommaso Di Noia,
Carlo Guarnieri Calò Carducci, *Student Member*, *IEEE* and Maurizio Spadavecchia, *Member, IEEE*
Department of Electrical & Information Engineering (DEI)
Politecnico di Bari
Via E. Orabona, 4 - 70125 Bari, Italy
[dinisio, guarnieri, spadavecchia]@misure.poliba.it, tommaso.dinoia@poliba.it

***Abstract* — This paper proposes an innovative method for power consumption measurement in microcontroller based systems, which provides high accuracy on a wide dynamic range of current values, resulting particularly suitable for all those applications characterized by alternating low/high-power modes and fast current variations. We demonstrate that using an op-amp based voltage feedback configuration, it is possible to use shunt resistor values higher than usual to obtain increased voltage drops without affecting the microcontroller's power supply voltage. Consequently, it is possible to directly use a DAQ board to acquire the shunt voltage, eliminating all those common errors, like offset and gain, due to the use of an additional intermediate amplification stage. The proposed scheme has been successfully used to accurately characterize the power consumption of a single sensor node of a Wireless Sensor Network (WSN).**

Keywords— Current Monitor; Microcontroller Consumptions; Sensor nodes; Wireless Sensor Network (WSN); Arduino; Internet of Things (IoT)

I. INTRODUCTION

The Internet of Things becomes every day more and more close. Whereas at present it is estimated that 99.4 % of the existing objects is yet unconnected (only 10^{10} of $1.5 \cdot 10^{12}$) [1], in the coming years it is expected a widespread distribution of network-connected devices, with a forecast of volumes that would justify the name, that some have attributed to, as *Internet of Everything*.

Bearing in mind the actual price of most microcontrollers [2] as well as of most common sensors, the lower limit to the cost of a remote measurement node is often dictated by the use of communication modules employing proprietary protocols, whose impact on the overall cost of the sensor node can vary from 50 % up to 90 %. On the other hand, more computational power becomes available with affordable costs, which extends the number of applications and algorithms that can be implemented on WSNs, such as image processing, surveillance, remote metering and industrial process control [3]-[9].

In this scenario, extremely low-power electronics are turning from desirable to mandatory and designers are requested to face a daily challenge in order to make the sensor nodes expected life specifications met. This goal is typically achieved by selecting the most appropriate components, by optimizing the code to reduce consumptions to a minimum and by managing the power supply of the devices' modules in a smart manner, for example by turning off the ADC and other modules except when required. But often the energy demand is still too high in the long run and, while waiting for the next generation of lithium-based batteries or new supercapacitors, the need for high capacity and durable batteries is being partially overcome by the spread of solutions for energy harvesting, which would allow to mitigate recharging issues in a world permeated by energy-hungry devices.

However, each of these solutions has to pass through a careful energy budget analysis. Often, is not possible to perform accurate simulations in order to balance the available or the harvestable energy with the requested one and, therefore, a precise experimental measurement of all time-variant contributions is required.

In this paper we propose a measurement scheme to fully characterize the dynamic current consumption of devices which alternate phases of extremely low consumption with phases in which higher currents flow through the load, with fast transitions. This is typical of microcontroller-based applications, especially those related to WSNs. The paper is structured as follows. In Sec. II the measurement principle is explained and compared with other methods. The implementation of the proposed approach is detailed in Sec. III, where simulations have been used to finely tune and verify the design. In Sec. IV, the experimental verification and comparison with other approaches in controlled test conditions is shown. Finally, in Sec. V, we report and compare power consumption measurements on one sensor node of the multipurpose WSN described in [10] and we propose an effective battery-consumption design formula.

II. Measurement Principle

There are several well-known techniques to measure currents in low-power applications. A wide compendium can be found in [11]-[13]. The measurement of average powers integrated in relatively large observation windows can practically be performed by using inexpensive digital multimeters [14][15]; a circuit topology using a current mirror and a capacitor is also known [16]. However, when fast current transitions should be observed, the technique generally used consists in high-rate sampling of the voltage of a shunt resistor; a different approach, proposed in [17], gives the per-cycle energy consumption of a CMOS microprocessor by measuring with a 60 MSPS 16-bit ADC the voltage drop of switched capacitors.

The simplest method (Fig. 1a) to measure the electrical current I_L flowing in a load consists in measuring the voltage drop V_{Sh} across a shunt resistor R_{Sh} connected in series between the power supply V_S and the same load, which is the approach followed in [18]-[20]. The shunt current $I_{Sh} = V_{Sh}/R_{Sh}$ is equal to I_L less than a generally negligible difference due to the finite impedance and bias current of the voltmeter.

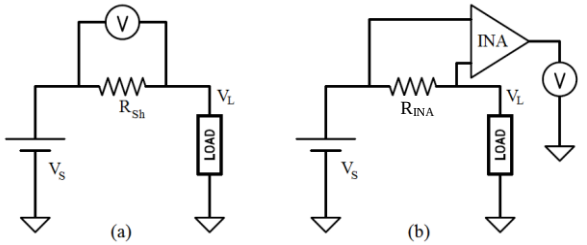

Fig. 1. (a) Simplest "shunt" measurement scheme, (b) improved "shunt + INA" measurement scheme

However this measurement scheme has a great limit: as the current increases, the shunt voltage also increases, decreasing the voltage on the load. When dealing with active loads like microcontrollers, this can lead to a measurement error due to the dependence of the supply current with the device operating voltage as for the case of the Atmel ATmega328P [21].

A possible solution is to use a current mirror [22], though it introduces a current copying error that may not be negligible over the entire measurement range. Another common approach (Fig. 1b), abbreviated here as "shunt + INA", consists in using a smaller shunt resistor R_{INA} to limit the related voltage drop and an instrumentation amplifier (INA) or operational amplifier to read the small shunt voltage, amplifying it by a given factor G [19], [23], [24]. It is $V_{INA} \cong G\, I_L R_{INA} + O$, where O is the offset introduced by the amplifier. However, in this case the so derived current measurement uncertainty is affected also by the uncertainties in the determination of the offset, u_O , and of the gain u_G.

Although this scheme has a lower impact on the load operating voltage, it still introduces new limiting factors, such as reduced bandwidth and input offset voltage. The former of course limits the frequency of observable signals, whereas the latter, if not accurately compensated, can make small currents measurement impossible. Indeed, since the input offset voltage of the instrumentation amplifier is typically in the range of tenth to hundreds of microvolts, it is mostly unfeasible to accurately read current values spread over several orders of magnitude, from tens of milliamps of a microcontroller in operating mode to a handful of microampere of a microcontroller in power-down state.

In order to overcome these limitations, we propose to use, for a different purpose, a modification of a well-known circuital topology that is at the base of constant current sources. The op-amp-based voltage-controlled current generator (Fig. 2a) is largely used to easily create a current sink/source, since its voltage follower configuration forces the input voltage over a known resistor R, so to generate the desired current.

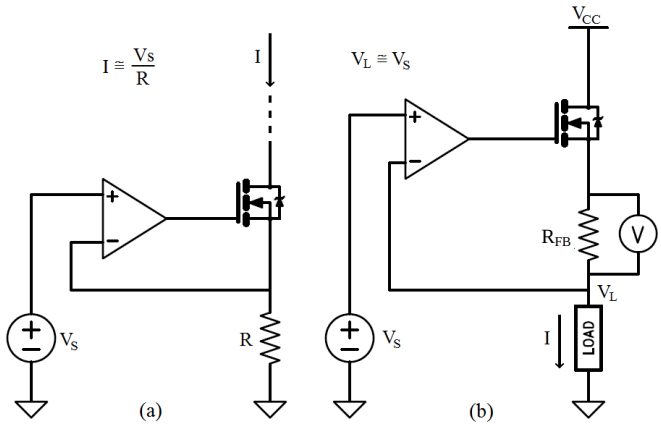

Fig. 2. Voltage-controlled current sink (a), proposed "shunt + feedback" method to measure the current in the load for a fixed operating voltage (b)

Exploiting the ability of the virtual short-circuit between terminals to maintain a fixed potential approximately equal to V_S at the op-amp inverting input, we put the load in place of R so to fix its operating voltage to a given value $V_L \cong V_S$. We then placed the shunt resistor R_{FB} in series with this node (Fig. 2b), whose voltage will add up to the load operating voltage. In this paper, we abbreviate this scheme as "shunt + feedback". This scheme can be seen also as a modification of the so called *feedback ammeter* [11], from which it differs for several aspects: the choose of a non-zero reference voltage, the measurement of the output as the voltage drop of the shunt resistor, and the presence of a transistor to control higher currents.

The clear advantage is thus to untie the tradeoff between the need to use larger resistors to detect small currents, and the necessity of not altering the voltage on the load, which would result in a perturbation of its operating condition and of its power consumption. In addition, in this configuration the op-amp input offset no longer affects the detectability of small currents, since it affects only the accuracy of the

voltage imposed to the load. Clearly the power supply voltage V_{CC} of this circuit should be greater than V_L to assure proper operation of op-amp and transistor and (similarly to the other methods) should take into account the voltage drop V_{Sh} on the shunt resistor. It should be noted that the use of higher supply voltages might be problematic for battery operation of WSN nodes; it is perfectly compatible, instead, during the design and characterization phase of nodes, when bench-top power supplies can be used. In addition, it should also be considered that it would be unfeasible in most cases for a sensor node to have available a dedicated high-precision and high-speed ADC for the real-time monitoring of its power consumptions, not mentioning the required storage space and computational power.

The op-amp model should be chosen in order to provide a sufficient bandwidth with respect to load current variations, a negligible input bias current with respect to the smallest expected load current and it should have rail-to-rail output to assure MOSFET gate driving capability.

III. Measurement Circuit Design and Simulation

The proposed method in Fig. 2b is, however, subject to the onset of oscillations due to the continuous change of the transistor bias point while the current drained by the load varies. The equivalent impedance of the load, especially in presence of large capacitive loads, interacts with the feedback loop, promoting the spreading of unwanted resonances that must be suppressed.

The design process has been conducted making use of PSpice tools for parametric simulations, in order to find the best values of compensation capacitors that provide stability over the range of interest.

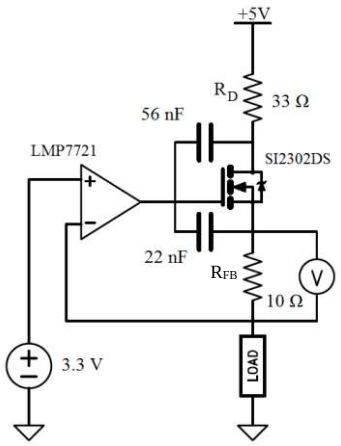

Fig. 3. Adopted circuit for the measurement scheme

The final circuit is reported in Fig. 3, where a resistor and two capacitors have been added to suppress the undesired oscillations in the working current range, which is 1 μA to $I_{MAX} = 30$ mA for the sensor node described in [10], with capacitive load up to 10 nF. The current range is shown in the simulation of Fig. 4, where the vertical line denotes the maximum current such that V_L remains nearly constant, $I_L \propto 1/R$ and the MOSFET remains in the saturation region. The derivative of I_L with respect to R, which is proportional to $1/R^2$, is also shown to emphasize the useful operating range.

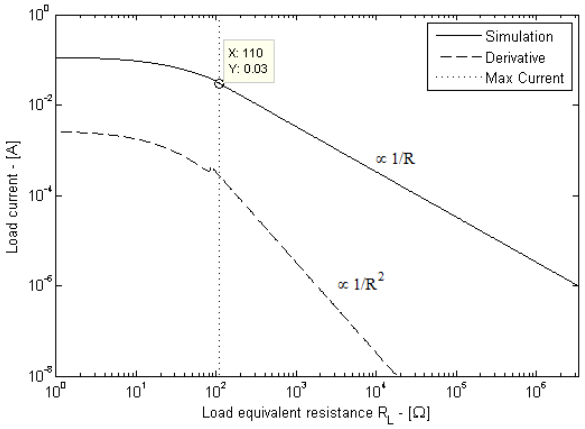

Fig. 4. Load current as a function of load resistance, obtained by means of a PSpice DC simulation. The derivative of the load current and the higher current limit are also indicated.

The chosen field-effect transistor was an NXP SI2302DS N-channel enhancement mode, which ensures fast switching time, a minimum threshold voltage V_{th} = 0.45 V and DC current drive capability up to 0.7 A. When dimensioning the circuit for a given maximum load current I_{MAX}, it is important that the resistors in Fig. 3 are chosen such that the voltage drop is compatible with the operation of the MOSFET in saturation mode, which gives constraints on gate-source voltage V_{GS} and on drain-source voltage V_{DS}. In particular, the gate voltage V_G, which cannot exceed V_{CC} if a rail-to-rail op-amp is used, should be such that $V_{th} < V_{GS}$, where $V_{GS} = V_G - V_L - R_{FB} \cdot I_L$. Moreover V_{DS}, which can be calculated as $V_{DS} = V_{CC} - V_L - (R_{FB} + R_D) \cdot I_L$ should be greater than the minimum value V_{DSmin} that can sustain the current I_{MAX}. The previous constraints are synthetized as:

$$\begin{cases} R_{FB} < \dfrac{V_{CC} - V_L - V_{th}}{I_{MAX}} \\ R_{FB} + R_D \le \dfrac{V_{CC} - V_L - V_{DS\,\min}}{I_{MAX}} \end{cases} \quad (1)$$

As regards the op-amp, we chose an electrometer-grade amplifier by Texas Instruments, model LMP7721. It assures an ultra-low input bias current of 3 fA (max 5 pA in all conditions) which is negligible when compared even on the smallest expected current flowing in the load. Moreover, it has a small input voltage noise of only 6.5 nV/√Hz, a wide-gain bandwidth GBW = 17 MHz, an average slew rate SR = 10 V/μs and output swing capabilities very close to rails, about 30 mV from positive and negative rails.

A simulation of transients has been conducted by switching a voltage-controlled resistor emulating a real load

varying from low to high consumption mode. The resistance range in the simulation was [110, 3.3e6] Ω , which, for the given load voltage of 3.3 V, corresponds to the DC linear current range previously identified. The signal applied to the voltage-controlled resistor is a square wave with a rise/fall time t_r = 500 ns, a delay t_d = 10 µs, a period of 200 µs and a duty cycle δ = 0.5. The results for two different capacitive loads, C_L = 1 nF and C_L = 16 nF, are reported in Fig. 5.

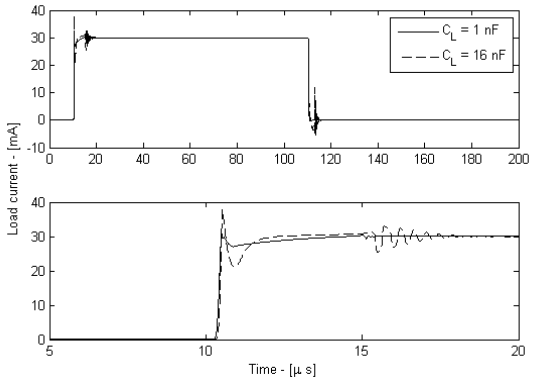

Fig. 5. PSpice transient simulation

As can be seen, for the larger value of capacitive load, an oscillation appears which, however, is dampened in a short time. It should be noted that, in several applications, the integral of the current is important in order to obtain the total charge or the energy of a given event, hence a small oscillation does not affect significantly the final result, as long as the DUT operation is not compromised.

IV. Experimental Validation

In this section an experimental comparison is presented of each one of the three methods listed in **Errore. L'origine riferimento non è stata trovata.**. Here we measure a current that is purposely controlled, while in Sec. V the current is sourced to an actual WSN node. The circuit validation has been performed in two different conditions, a static and a dynamic one, similarly to the simulations described in the previous section.

The operating voltage of the load was set to $V_L \cong V_S$ = 3.3 V.

For the instrumentation amplifier based method, we selected the INA225, a programmable-gain voltage-output current-shunt monitor by Texas Instruments, with a bandwidth of up to 250 kHz and a maximum gain error e_G = ± 0.3 %.

Shunt and load voltages have been measured using a NI USB-6361 X Series DAQ board by National Instruments, with eight 16-bit fully differential analog input channels able to provide sample rates up to 2 MS/s for single-channel acquisitions and up to 0.5 MS/ch/s for two-channel acquisitions [26].

Before proceeding with the tests, we accurately performed a 4-wire shunt resistance measurement for each of the three methods using a 3458A 8½ Digit - Digital Multimeter by Agilent Technologies, which has a maximum sensitivity of 10 µΩ. The resistance values are given in TABLE I. , measured with an integration time of 4 s, corresponding to a Number of Power Line Cycles NPLC = 200.

TABLE I.
Shunt Resistance Measurement

Symbol	Method	Nominal [Ω]	Measured [Ω] @ T_{amb} = 20°C
R_{Sh}	Shunt only	10	9.896
R_{INA}	Shunt + INA	1	1.0003
R_{FB}	Shunt + feedback	10	9.971

A. Static Test

In order to compare the three methods for different currents flowing in a load we selected five different load resistors with nominal values logarithmically spread over the DC linear range defined in the previous section. A 4-wire measurement of their value, similarly to the shunt resistors measurement, has been conducted and results are reported in TABLE II. for the sake of clarity.

TABLE II.
Load Resistors

Symbol	Nominal [kΩ]	Measured [kΩ] @ T_{amb} = 20°C
R_{L2}	0.1	0.09925
R_{L3}	1	0.9979
R_{L4}	10	9.908
R_{L5}	100	98.98
R_{L6}	1000	984.7

The compared measurement schemes are described in Figs. 1 and 2. For each scheme, the test procedure consists in the following steps: *(i)* change the load resistor; *(ii)* wait 10 s to assure that no transient behavior is present; *(iii)* perform 1 s data acquisition at 10 kS/s to measure voltages across both the shunt and load resistors. In order to maximize the input resolution for each method, a different input range and hence a different DAQ internal gain has been set for each method, according to the maximum expected voltage (see TABLE III.).

TABLE III.
DAQ Input Channels Configuration

Method	V to I_{Sh} Conversion Factor	Shunt max Voltage [a] [V]	DAQ Input Range [V] Shunt	Load
Shunt only	$1/R_{Sh}$	0.3	[-0.5 0.5]	[-5 5]
Shunt + INA[b]	$1/(G \cdot R_{INA})$	3	[-5 5]	[-5 5]
Shunt + Feedback	$1/R_{FB}$	0.3	[-0.5 0.5]	[-5 5]

[a] Expected maximum shunt voltages are calculated considering a current I_L = 30 mA
[b] The INA225 current monitor has been configured for a gain G = 100

The sampling frequency of the NI-USB-6361 DAQ for the static test has been kept deliberately low to ensure sufficient

settling time in the multi-channel acquisitions with non-simultaneous sampling, where the analog font-end may change its gain while scanning channels having different voltages and source impedances [26].

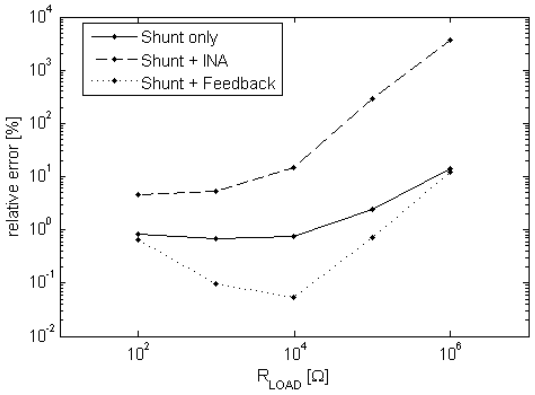

Fig. 6. Comparison of DC current measurement relative error

The results of Fig. 6 have been obtained by comparing the expected values I_L of the current flowing in the load with the current I_{Sh} flowing in the shunt, for each value R_{Ln} in TABLE II. For the scheme in which only the shunt is used, it is

$$I_L = \frac{V_L}{R_{Ln}}$$
$$I_{Sh} = \frac{V_{Sh}}{R_{Sh}} \qquad (2)$$
$$e_{\%} = \frac{I_{Sh} - I_L}{I_L} \cdot 100$$

where V_L and V_{Sh} are respectively the measured voltage across the load and the shunt resistor. For the other schemes, the calculation of I_{Sh} changes accordingly to the conversion factor indicated in TABLE III. The proposed method shows excellent accordance with the expected values of the current flowing in the load, with reduced errors compared to the other methods. It has also the clear advantage of maintaining V_L fixed to V_S for all the values of current in the load, as is illustrated in Fig. 7.

In should be noted from Fig. 6 that the "shunt + INA" method produces higher relative errors due to gain error, offset error and output swing of the amplifier, the last two factors being particularly significant when small currents, corresponding to high load resistances, are considered. The errors of the "shunt + feedback" and "shunt only" methods are mainly due to the errors of shunt resistance and shunt voltage measurements. Instead, the feedback design and the transistor characteristics affect mainly V_L fixing capability and dynamic performance. For small currents, a similar error increase for both methods can be ascribed to the relative error of the DAQ board, which increases for the small voltages developed across the 10 Ω shunt resistor. For other current values, the observed differences between the two methods are probably due to the different impedance values seen from the high voltage node of the shunt resistor toward ground, which affect the measurement error of the DAQ board [26]. That difference fades away for higher currents because the transistor bias point moves in the linear region, leading to a drastic decrease of the channel impedance, a condition comparable with the "shunt only" method in which the impedance toward ground is virtually zero trough the positive terminal of the power supply.

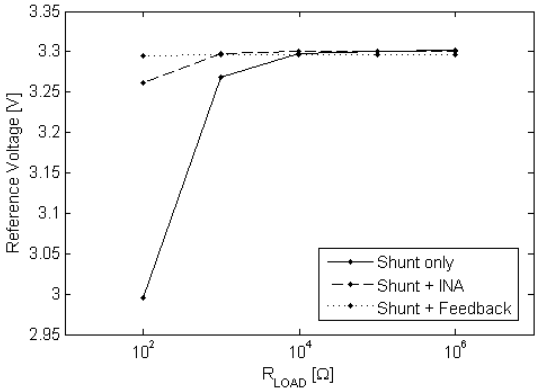

Fig. 7. Comparison of reference voltage V_L

B. Dynamic Test

For this test we used a MCP4131 7-bit digital potentiometer by Microchip, with a total resistance of 100 kΩ, to emulate a fast switching load from a low power condition in which it consumes approximately $V_L/100\ k\Omega \approx$ 30 μA, to a high power state in which it absorbs $V_L/100\ \Omega \approx$ 30 mA. An Arduino UNO board [2] was also used to control the digital potentiometer through SPI communication, switching from highest to lowest resistance value and vice versa every 100 μs.

Since this test is ran at the maximum available DAQ sampling frequency f_s = 500 kS/s in order to detect possible ringing, it does not make sense to report a quantitative analysis because DAQ requested settling times for multichannel measurement are not met and it would result in a great measurement error especially for low currents. On the other hand, this test shows the dynamic capability of the measurement setup to maintain a fixed voltage reference even during typical fast switching events.

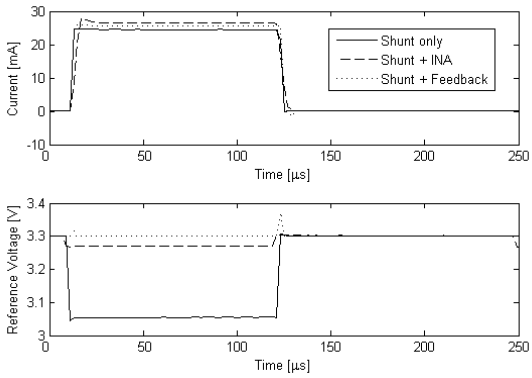

Fig. 8. Comparison of dynamic responses for the three methods

A small capacitive load C_L = 100 pF has been added during the test in parallel to the load resistor in order to provide a minimal load without interfering with the small low-power state current.

As it is evident from Fig. 8, the reference voltage V_L applied to the load exhibits a very fast spike (<2 μs) during load transitions in the proposed scheme, which still provides excellent stability overall when compared to the other methods for the entire duration of the test.

V. Real-Case Application

The proposed technique was applied to the study of energy consumption of the WSN framework described in [10]. This section is structured as follow: in V.A the WSN node and its operating modes are briefly reviewed; in V.B an energy characterization is performed with the proposed technique; finally in V.C the previous characterization data are used to provide a design formula which allows one to choose the set of the WSN operating parameters for a given energy constraint.

A. WSN

The WSN, depicted in Fig. 9, relies on the use of an nRF24L01+ wireless modules by Nordic Semiconductor and an ATmega328P microcontroller, found also in the Arduino UNO board [2], to implement each sensor node. This design was motivated by the necessity of having low costs for the deployed network, while moving complexities to the central server, where more powerful hardware is easily available and its cost might be spread across several different applications. The proposed system can be used in different fields ranging from education [27]-[28] to automotive [29], environment [3], energy monitoring [30]-[31], automation and robotics.

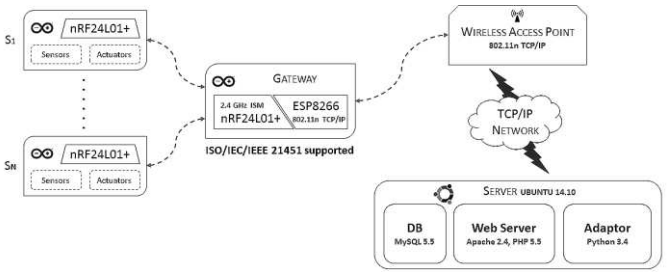

Fig. 9. Network architecture

In general, when no measurement or transmission activity is required, the microcontroller and the wireless module should be in the lower admissible power consumption mode. The microcontroller runs at 1 MHz and, to save energy, it is put into *power-down* mode with the possibility of being awakened in two different ways: periodically by the internal watchdog, in a sensor configuration we call *Tx mode*; or upon reception of an external interrupt from the wireless module, in the *Rx mode* configuration. In the former case, the wireless module is in *power-down* and is awakened by the microcontroller; in the latter case it is *standby-I mode*, and is awakened upon reception of a radio packet. Furtherly, a third operational mode of the sensor node, *TxRx mode*, is also taken into consideration for a mixed behavior. A summary of all designed energy saving combinations for the microcontroller and the wireless module and respective current consumption measurements are reported in TABLE IV. Since these measurements are relative to stationary energy saving operation, which can be artificially prolonged for an indefinite time, they have been performed with a high precision multimeter. To extend the characterization to the other operating phases of the sensor node, characterized by fast variations of current consumption, we have used the proposed method, as illustrated in the following subsection.

TABLE IV.
Sensor Node Modes and Current Consumptions[a] [b]

Sensor mode	ATmega328P		nRF24L01+	
	Mode	Current [μA]	Mode	Current [μA]
Tx	Pwd/Wdt	4.38	Pwd	1.13
Rx	Pwd/Int	0.106	Standby-I	25.4
TxRx	Pwd/Wdt+Int	4.38	Standby-I	25.4

[a] Measured using an Agilent 3458A multimeter

[b] *Pwd* stands for *power-down*; *Wdt* and *Int* mean, respectively, that the internal wake-up on *watch-dog* and on *pin interrupt* are active

B. Energy consumption

Observing energy consumption in real operating conditions required a high current measurement rate. Indeed, when the sensor node is configured to work in Tx mode, the microcontroller wakes up when the configured watchdog interval is elapsed, then checks if the desired interval between transmissions is also elapsed. If so, it completes the procedure transmitting a 32-byte packet at 2 Mbps on-air data-rate before returning to sleep mode. Hence, in Tx mode

the sensor node has three operating phases: power-down of both microcontroller and wireless module, wake-up on watchdog and transmission, to which is added a fourth survey phase (data acquisition and processing) that has been measured separately for a typical procedure, consisting in one ADC sampling and three floating point operation for data conversion.

The measurements performed with the proposed method on a sensor node working in Tx mode are shown in Fig. 10, where the fast transition of current in the watchdog and transmission windows can be appreciated.

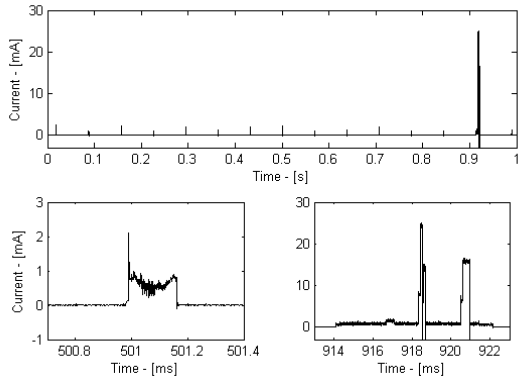

Fig. 10. Sensor node current measured with the proposed method (top), zoom of one of the many watch-dog events (left), which repeat every 64 ms, and zoom of a data transmission event (right). The entire cycle repeats every one second.

In order to compare performance of the three methods, we used them to measure the sensor node current at $f_s = 1$ MS/s sampling frequency, obtaining three vectors $\mathbf{I}_{Sh} = [I_{Sh,1}, \dots, I_{Sh,N}]$ of N measurements of the shunt current I_{Sh}, with $N = 10^8$, corresponding to a 100 s observation window (see Fig. 11a for a one second subset). This was an accelerated test, because transmissions were set to a relatively high frequency, 1 Hz.

Since this large data set contained hundreds of events, an automatic segmentation algorithm was developed to identify the operating phases of the sensor node in Tx mode, so allowing one to calculate energy consumption for each phase: power-down, wake-up on watchdog and transmission.

The segmentation algorithm consists in the following steps, which are repeated for each measurement method.

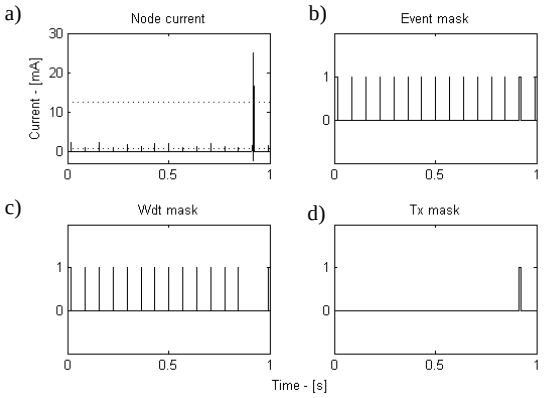

Fig. 11. a) Sensor node current consumption (solid line) measured with the proposed method and thresholds (dotted lines); b) event mask; c) Wdt mask; d) Tx mask

Firstly, a low threshold $th_1 = std(\mathbf{I}_{Sh})$ and a high threshold $th_2 = \max(\mathbf{I}_{Sh})/2$ are calculated from the $\mathbf{I}_{Sh}$ vector and used to calculate two raw logical masks:

$$\begin{aligned} \mathbf{M}_1 &= \mathbf{I}_{Sh} > th_1 \\ \mathbf{M}_2 &= \mathbf{I}_{Sh} > th_2 \end{aligned} \tag{3}$$

where the greater-than operator is applied to each element of $\mathbf{I}_{Sh}$, so obtaining Boolean vectors $\mathbf{M}_1$ and $\mathbf{M}_2$ of size N. Ideally, a given element of $\mathbf{M}_2$ is true when the corresponding element of $\mathbf{I}_{sh}$ is relevant to a measurement performed when the sensor node is transmitting. Analogously, a given element of $\mathbf{M}_1$ is true when the sensor node is not in power-down. These masks may still contain holes inside the event windows because of current fluctuations around the thresholds. Thus the final event mask $\mathbf{M}_{\text{EVENT}}$ (Fig. 11b), which individuates the instants in which the sensor node is not in power-down, is derived from $\mathbf{M}_1$ using a morphological closing operation [32] which consists in a dilation operation $\oplus$ with a structuring element SE_1 large 300 μs followed by an erosion $\ominus$ with the same structuring element

$$\mathbf{M}_{\text{EVENT}} = \mathbf{M}_1 \bullet \mathbf{SE}_1 = (\mathbf{M}_1 \oplus \mathbf{SE}_1) \,!\, \mathbf{SE}_1 \tag{4}$$

A dilation operation process also applies to $\mathbf{M}_2$ with a larger 50 ms structuring element $\mathbf{SE}_2$, so obtaining a mask $\mathbf{M}_3$ around higher consumptions instants due to transmission. A logical *and* operation, $\wedge$, with $\mathbf{M}_{\text{EVENT}}$ is performed in order to individuate the entire transmission phases, which are characterized by an alternation of higher and lower currents, so obtaining the final transmission mask $\mathbf{M}_{\text{TX}}$ (Fig. 11d)

$$\begin{aligned} \mathbf{M}_3 &= \mathbf{M}_2 \oplus \mathbf{SE}_2 \\ \mathbf{M}_{\text{TX}} &= \mathbf{M}_{\text{EVENT}} \wedge \mathbf{M}_3 \end{aligned} \tag{5}$$

Two more masks, power-down $\mathbf{M}_{\text{PWD}}$ and watchdog event $\mathbf{M}_{\text{WDT}}$ (Fig. 11c) are obtained as follows

$$\begin{aligned} \mathbf{M}_{\text{PWD}} &= \neg\mathbf{M}_{\text{EVENT}} \\ \mathbf{M}_{\text{WDT}} &= \mathbf{M}_{\text{EVENT}} \text{ XOR } \mathbf{M}_{\text{TX}} \end{aligned} \quad (6)$$

We used the above-defined masks to perform a numerical integration of the current I_{Sh} for transmission and watchdog events, in order to compute the average and the standard deviation of the requested charge per event, whose values will be expressed in [Ah] instead of coulombs [C], to simplify their comparison with batteries' capacity. Considering, for example, the computation of the transmission charge, firstly the transmission events are searched by individuating all the connected components [32] in which $\mathbf{M}_{TX}$ is true, so obtaining M set of indices $C_1, \dots, C_M$, where M is the number of events. The charge of the m-th event is then $Q_{Tx,m} = \frac{1}{f_S}\sum_{i\in C_m} I_{Sh,i}$, from which average and standard deviation of the M events is easily calculated. The charge of watchdog events is calculated similarly by using $\mathbf{M}_{WDT}$.

The integration results are reported in Fig. 12 with a comparison of the three measurement methods; statistics have been computed over 90 identified transmission events and 1441 identified watchdog events. The measured average power-down current has been multiplied, for comparison purposes, by one hour and reported in Fig. 12 in [mAh] units. These results provide the parameters reported in TABLE V of Sec. V.C, which are necessary for the design formula proposed in that section.

Measured values show that no data are available for watchdog events with INA method, since it was not able to detect any one. The mean values for the Tx event confirm that the simple shunt technique tends to underestimate the real current consumption since the voltage drop over the shunt resistor decreases the operating voltage and hence the drained current. On the other side, the corresponding value measured with the INA method is consistent with its 5 % overestimation error for high currents, already shown in Fig. 6.

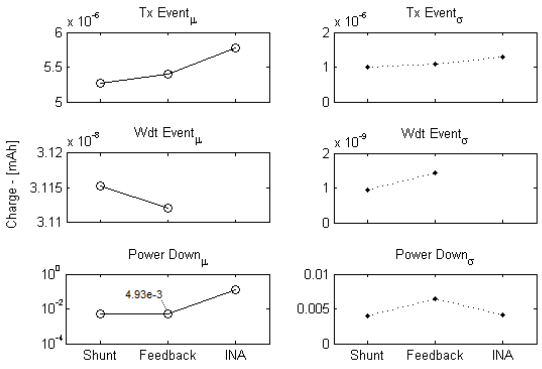

Fig. 12. Mean values μ of requested charge in different operating phases and respective standard deviations σ. In each plot, the reported measurements (from left to right) refers respectively to shunt only, shunt + feedback and shunt + INA methods.

Even if the 16-bit DAQ board has for the proposed method a current resolution of 1 LSB ≈ 1.5 μA over the specified range, the measured value of power-down current $I_{PWD,Tx}$ = 4.93 μA (Fig. 12) is very close to the total one reported in TABLE IV. of 5.51 μA, whereas its standard deviation is σ ≈ 4 LSB. In fact, using this method the main limit appears to be the performance of the available DAQ. Instead, the power-down current measured with the INA method is two orders of magnitude far from the actual value and near the lower bound of the output swing of that amplifier.

TABLE V.
SYMBOLS, VALUES AND DESCRIPTION OF DESIGN PARAMETERS

Symbol	Value		Description
$I_{Pwd,Tx}$	4.93	[μA]	Power-down current, sensor in Tx mode[a]
$I_{Pwd,Rx}$	25.4	[μA]	Power-down current, sensor in Rx mode[a]
$I_{Pwd,TxRx}$	30.3	[μA]	Power-down curr., sensor in TxRx mode[a]
Q_{Wdt}	31.12	[pAh]	Watchdog Event
T_{Wdt}	0.016 – 8	[s]	Watchdog Interval
Q_{Tx}	5.4	[nAh]	Transmission Event
T_{Tx}	-	[s]	Transmission Interval
N_{Tx}	-	-	Number of 32-byte packets
I_{Op}	798	[μA]	Operating Event [b] [c]
T_{Op}	1.795	[ms]	Operating Time [c]
N_{Op}	-	-	Number of Operations
I_S	-	-	Sensor circuitry current

a. Combined microcontroller and wireless module power-down current

b. Measured with an Agilent 3458A 8½ digital multimeter

c. The operation consists of 1 ADC conversion and 3 floating-point calculations. The time was calculated as the average of a loop containing 100 such operations.

C. Battery consuption desigin formula

In order to complete the energy analysis for the sensor node, a battery consumption design formula was derived based on current measurements. The measurements obtained in the previous section with the proposed method for Tx mode have been reported in TABLE V. in addition to the measurements for Rx and TxRx modes. TABLE V. lists also other parameters that fix sensor node operation other than time interval between transmissions T_{Tx} and number of bytes transmitted N_{Tx}. In particular, a sensor node task model is used in which, before each transmission, N_{Op} operations are performed, each one having duration T_{Op}, microcontroller current I_{Op} and involving sensor circuitry current I_S. Data of TABLE V can be used together with the following simple design formula to evaluate the hourly battery consumption of a WSN node based on the proposed framework

$$\begin{aligned} Q_h = (1\,\text{h})\cdot I_{Pwd} + \frac{1\,\text{h}}{T_{Wdt}}\cdot Q_{Wdt} + \\ \frac{1\,\text{h}}{T_{Tx}}\cdot\left[N_{Tx}\cdot Q_{Tx} + N_{Op}\cdot T_{Op}\cdot(I_{Op}+I_S)\right] \end{aligned} \quad (7)$$

where I_{Pwd} is one of the values $I_{Pwd,Tx}$, $I_{Pwd,Rx}$ or $I_{Pwd,TxRx}$ from TABLE V.

The expected sensor node lifetime L_{Exp} in hours is very simple to calculate using the given formula, since it only implies a division by the adopted battery capacity Q_{Batt}

$$L_{Exp} = Q_{Batt}/Q_h \ \text{[h]} . \quad (8)$$

Of course the designer may use this information choosing the transmission intervals to obtain longer lifetimes, or different techniques can be exploited, such as those based on wireless power transmission [33] and energy harvesting from photovoltaic and thermoelectric generators [34] to charge the battery while the sensor is in power-down.

The given design formula is a simplified expression that tends to under estimate the expected lifetime in conditions of highly intensive operations, since the power-down current should be multiplied by 1 hour less the sum of all other events duration. Furthermore, asynchronous occasional Rx events of the wireless module are considered negligible with respect to the overall current consumption; if this is not the case, an Rx event probability density function may be used to take into account also this contribution.

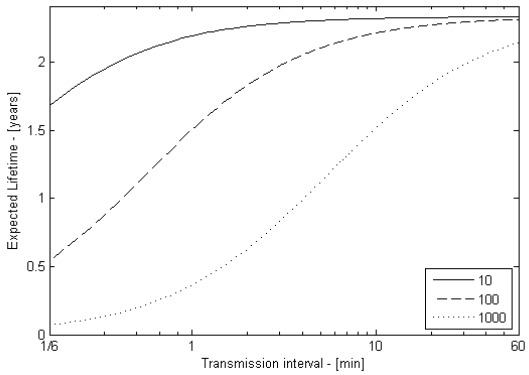

Fig. 13. Sensor node expected lifetimes versus transmission intervals for three different values of averaged ADC readings per sensor.

Just to give a brief idea of its application, we considered a sensor node in TxRx mode powered by a CR2450 coin-cell battery (620 mAh of nominal capacity) with five different resistive sensors. Each one is powered through a microcontroller pin and read using a voltage divider with 10 kΩ total resistance, thus the sensor circuitry current for a 3.3 V operating voltage is I_S = 330 μA when the pin output is high. Computed expected lifetimes are reported in Fig. 13 for different intervals between data transmission events and for a different number of averaged ADC readings per sensor. More than two years of battery operation can be easily reached when each transmitted value is the mean of 10 sensor readings; when 100 sensor readings are averaged, the transmission interval should be at least 3 minutes to obtain a two years lifetime.

CONCLUSION

We have presented an innovative high precision method for microcontrollers' current consumption measurement. It was validated by means of static and dynamic tests that showed its capability to keep the load operating voltage fixed during the measurement process. In comparison, the use of a simple shunt resistor and the use of an instrumentation amplifier pose the following limitations. From one end, the requirement of measuring large as well as small currents flowing into small shunt resistors leads to the use of high-gain instrumentation amplifiers, which however introduce inaccuracies particularly apparent at the lower bound of the measurement range. From the other end, the voltage drop on large shunt resistors changes the voltage supply of the DUT resulting, in the case illustrated in this paper, in consumption under-estimation.

The method was applied to power consumption measurement of a sensor node based on a previously proposed WSN framework, applicable in different application contexts. Developed by using open source software and readily available electronic modules and in spite of its low cost, it permits the bidirectional communication and the report of asynchronous events to connected users. An algorithm for the segmentation of the measured current waveform in order to identify the different operating phases of the sensor node was also described, and was used to identify its power consumption model. A detailed battery consumption analysis was carried out, which confirmed the possibility of life-long operation.

REFERENCES

[1] J. Bradley, J. Barbier, D. Handler, "Embracing the Internet of Everything to capture your share of $14.4 trillion," White paper, Cisco, 2013.

[2] Arduino website, www.arduino.cc, visited June 25, 2015.

[3] F. Adamo, F. Attivissimo, C. Guarnieri Calò Carducci, A. M. L. Lanzolla, "A smart sensor network for sea water quality monitoring," IEEE Sensors Journal, vol. 15, pp.2514-2522, May 2015.

[4] M. Rahimi, R. Baer, O. I. Iroezi, J. C. Garcia, J. Warrior, D. Estrin, and M. Srivastava, "Cyclops: in situ image sensing and interpretation in wireless sensor networks," in Proc. 3rd Int. Conf. on Embedded networked sensor systems (SenSys '05), San Diego, Nov. 2-4, 2005, pp. 192-204.

[5] F. Adamo, F. Attivissimo and A. Di Nisio, "Calibration of an inspection system for online quality control of satin glass," IEEE Trans. on Instr. and Meas., vol. 59, no. 5, pp. 1035-1046, May 2010.

[6] L. Ferrigno, V. Paciello, A. Pietrosanto, "Visual sensors for remote metering in public networks," IEEE Instrumentation and Measurement Technology Conference (I2MTC), Binjiang, 10-12 May 2011, pp-1-6.

[7] F. Adamo, F. Attivissimo, L. Fabbiano, N. Giaquinto, M. Spadavecchia, "Soil moisture assessment by means of compressional and shear wave velocities: Theoretical analysis and experimental setup," Measurement: Journal of the International Measurement Confederation, vol. 43, no. 3, pp. 344-352, April 2010.

[8] A. Lay-Ekuakille and A. Trotta, "Predicting VOC Concentration Measurements: Cognitive Approach for Sensor Networks," IEEE Sensors Journal, vol. 11, no. 11, pp. 3023-3030, Nov. 2011.

[9] V.C. Gungor, G.P. Hancke, "Industrial wireless sensor networks: challenges, design principles, and technical approaches," IEEE Trans. on Industrial Electronics, vol.56, no.10, pp.4258-4265, Oct. 2009.

[10] A. Di Nisio, T. Di Noia, C. Guarnieri Calò Carducci, M. Spadavecchia, "Design of a low cost multipurpose wireless sensor network," in proc. IEEE Int. Workshop on Measurements & Networking (M&N), pp.1-6, 12-13 Oct. 2015. doi: 10.1109/IWMN.2015.7322986.

[11] "Low level measurement handbook," Keitley Instruments Inc., 7th ed., 2013.

[12] T. Regan, J. Munson, G. Zimmer, M. Stokowski, "Current Sense Circuit Collection," Linear technology corporation, AN 105, Dec. 2005.

[13] A. Moschitta, I. Neri, "Power consumption Assessment in Wireless Sensor Networks," in *ICT - Energy - Concepts Towards Zero - Power Information and Communication Technology*, InTech, 2014, ch. 9, ISBN 978-953-51-1218-1

[14] D. Macii, D. Petri, "An Effective Power Consumption Measurement Procedure for Bluetooth Wireless Modules," IEEE Trans. on Instr. & Meas., vol.56, no.4, pp.1355-1364, Aug. 2007.

[15] D. Macii, D. Petri, "Accurate Software-Related Average Current Drain Measurements in Embedded Systems," IEEE Trans. on Instr. & Meas., vol.56, no.3, pp.723-730, June 2007.

[16] V. Konstantakos, K. Kosmatopoulos, S. Nikolaidis, T. Laopoulos, "Measurement of Power Consumption in Digital Systems," IEEE Trans. Instrum.& Meas., vol. 55, no. 5, pp. 1662-1670, Oct. 2006.

[17] N. Chang, K. Kim, H. G. Lee "Cycle-accurate energy measurement and characterization with a case study of the ARM7TDMI," IEEE Trans. on VLSI Systems, vol. 10, no. 2, pp. 146-154, April 2002.

[18] N. Zhu, I. O'Connor, "Energy measurements and evaluations on high data rate and ultra low power WSN node," in Proc. 10th IEEE Int. Conf. in Networking, Sensing and Control (ICNSC), Evry, 10-12 April 2013, pp.232-236.

[19] E. Casilari, J. M. Cano-Garcia, G. Campos-Garrido, "Modeling of Current Consumption in 802.15.4/ZigBee Sensor Motes," Sensors, vol. 10, pp. 5443-5468, June 2010.

[20] J. P. Amaro, R. Cortesao, J. Landeck, F.J.T.E. Ferreira, "Harvested Power Wireless Sensor Network Solution for Disaggregated Current Estimation in Large Buildings," IEEE Trans. Instrum.Meas., vol.64, no.7, pp.1847-1857, July 2015.

[21] Atmel ATmega328P 8-bit Microcontroller datasheet, p. 598, online: http://www.atmel.com/images/Atmel-8271-8-bit-AVR-Microcontroller-ATmega48A-48PA-88A-88PA-168A-168PA-328-328P_datasheet_Complete.pdf

[22] T. Laopoulos, P. Neofotistos, K. Kosmatopoulos, and S. Nikolaidis, "Measurement of current variations for the estimation of software-related power consumption," IEEE Trans. Instrum.& Meas., vol. 52, no. 4, pp. 1206–1212, Aug. 2003.

[23] A. Hergenroeder, J. Wilke, D. Meier, "Distributed Energy Measurements in WSN Testbeds with a Sensor Node Management Device (SNMD)," in *23rd Int. Conf. on Architecture of Computing Systems (ARCS)*, 22-23 Feb. 2010, pp. 1-7.

[24] L. Barboni, M. Valle, "Experimental analysis of wireless sensor nodes current consumption," in Proc. 2nd Int. Conf. on Sensor Technologies and Applications, Cap Esterel, Aug. 2008, pp. 401-406.

[25] J. Choma, Wai-Kai Chen, "Feedback Networks: Theory and Circuit Applications," World Scientific, 2007. ISBN 9810227701

[26] National Instruments NI-6361 DAQ datasheet, p. 7, online: http://www.ni.com/datasheet/pdf/en/ds-151

[27] M. Chirico, A. M. Scapolla, A. Bagnasco, "A new and open model to share laboratories on the Internet," IEEE Trans. on Instr. & Meas., vol. 54, June 2012, pp. 1111-1118.

[28] F. Adamo, F. Attivissimo, G. Cavone, N. Giaquinto, "SCADA/HMI systems in advanced educational courses," IEEE Trans. on Instrum. Meas., vol. 56, pp. 4-10, Feb. 2007.

[29] D. I. Katzourakis, E. Velenis, D. A. Abbink, R. HAppee, E. Holweg, "Driver's arms time-variant neuromuscolar admittance during real car test-track driving," IEEE Trans. on Instr. & Meas., vol. 63, pp. 221-230, Jannuary 2014.

[30] W. Chuyuan, L. Yongzhen, "Design of energy consumption monitoring and energy-saving management system of intelligent building based on the Internet of things," 2011 International Conference on Electronics, Communications and Control (ICECC), 9-11 Sept. 2011, pp. 3650-3652.

[31] F. Adamo, F. Attivissimo, A. Di Nisio, M. Savino, M. Spadavecchia, "A spectral estimation method for nonstationary signals analysis with application to power systems," Measurement, vol.73, pp 247-261, Sept. 2015.

[32] R. C. Gonzalez, R. E. Woods , "Digital Image Processing," 3rd ed, Prentice Hall, 2008.

[33] L. Angrisani, G. D'Alessandro, M. D'Apuzzo, M. D'Arco, "Enabling induction and wireless power transmission technologies aimed at supplying remote equipment in critical logistic scenarios," IEEE International Workshop on Measurements and Networking Proceedings (M&N), 7-8 Oct. 2013, pp.184-188.

[34] F. Attivissimo, A. Di Nisio, A.M.L Lanzolla, M. Paul, "Feasibility of a photovoltaic–thermoelectric generator: performance analysis and simulation results," IEEE Trans. on Instr. & Meas., vol.64, no.5, pp.1158,1169, May 2015.